Electrohydrodynamic generation of atmospheric turbulence

Yuan Yao* and Jesse Capecelatro
Department of Mechanical Engineering, University of Michigan, Ann Arbor, Michigan 48105, USA

(Received 5 February 2019; published 18 December 2019)

Ionization produced by cosmic rays and atmospheric radioactivity creates charged short life-time aerosol droplets in the upper troposphere. Inhomogeneities in the spatial distribution of aerosol droplets lead to time-varying electric fields and space charge, which can often be amplified by more than three orders of magnitude in extreme conditions, such as thunderstorms. The nonlinear coupling between ionized air, charged aerosol droplets, and the background electric field can result in electrohydrodynamic body forces that augment atmospheric turbulence. In this paper, a theoretical and numerical study on the electrohydrodynamic generation of atmospheric turbulence under fair weather and thunderstorm conditions is presented. Linear stability shows that coupling between ionized air and a background electric field acts to increase turbulent kinetic energy (TKE) in the upper troposphere, albeit over long time durations. Direct simulations of charged droplets in homogeneous shear flow demonstrate a nonlinear feedback mechanism capable of accelerating the growth rate. Streamwise velocity gradients induce fluctuations in droplet concentration and electric potential, resulting in a body force that generates vertical velocity fluctuations. Pressure strain then transfers this energy to turbulent fluctuations in the streamwise direction and the process repeats. This feedback mechanism was found to augment TKE at late stages of the shear layer growth.

DOI: 10.1103/PhysRevFluids.4.123701

I. INTRODUCTION

Ionization produced by cosmic rays and atmospheric radioactivity creates charged short life-time aerosols that have significant spatial and temporal variations in the troposphere [1–4]. In extreme conditions, such as thunderstorms, this variability has been observed to amplify the local electric field strength in the atmosphere by more than three orders of magnitude compared to typical fair weather conditions [5,6]. In the presence of a background electric field, gradients in space charge generate an electrohydrodynamic (EHD) body force if the gas is ionized. The EHD force that arises due to coupling between an electric field, ionized air, and charged aerosols has been shown experimentally to produce instabilities that trigger the onset of turbulent motion in quiescent aerosol clouds [7]. While EHD instabilities are known to induce turbulence in ionized fluids, such as electrolytic cells [8], liquid films [9], and electrostatic precipitators [10], and similar instabilities due to magnetohydrodynamics exist in plasmas [11–13], its role in augmenting atmospheric turbulence is less established.

Recent studies have shown that detailed interactions between turbulence and aerosol droplets can give rise to preferential concentration of charged particles capable of self-inducing atmospheric electricity [14,15], which might amplify the aforementioned effects. Depending on the sign and magnitude of the charge each particle carries, these self-induced electrical fields can either mitigate or enhance the level of clustering [15–17]. Preferential concentration describes the accumulation

*yyaoaa@umich.edu

of inertial (heavy) particles or droplets away from highly vortical regions of the turbulent flow [18–22]. When the timescale of the particles is on the same order as the turbulent eddies, particles are directed by coherent vortical structures to create nonhomogeneities in concentration and the onset of clusters. In the presence of gravity, preferential concentration by turbulence has been observed to cause particles to accumulate near the downward moving side of vortices where the fluid velocity aligns with the direction of gravity [23–25]. The gravitational settling of aerosol particles can be enhanced by this preferential sweeping mechanism by as much as 50% [24]. The collision rate between monodisperse particles is also considerably lower when gravity is present [26].

Wind shear (mean velocity gradient) ranging from $O(10^{-3})$/s to $O(1)$/s is common in the atmosphere [27–29]. When particles or droplets are placed within a mean velocity gradient, the anisotropy of the velocity fluctuations induces a preferential orientation of particle clusters and modifies their turbulent transport characteristics [30,31]. Recently, a new preferential concentration-driven instability has been identified for inertial particles suspended in sheared turbulence [32], showing that two-way coupling between the phases in the presence of mean shear and gravity can lead to the onset of turbulence.

The motivating hypothesis of the present study is that charged aerosols within the atmosphere couple nonlinearly with the background electric field and ionized air, resulting in the production of TKE. We refer to this as a three-way coupling process, whereby velocity fluctuations induce nonhomogeneities in droplet concentration, resulting in gradients in electric potential that increase the electric field strength and in turn amplify the gas-phase velocity fluctuations. We seek to identify under what conditions EHD-induced turbulence is relevant. To this end, a linear stability analysis is performed for sheared flow in the presence of a background electric field to understand the stability criteria, relevant nondimensional numbers, and timescales associated with EHD-induced turbulence. Then direct numerical simulations are carried out with relevant atmospheric parameters at 6 km altitude to understand the effect of added nonlinearity by aerosol dynamics on turbulence generation. The TKE budget and growth rate are then reported to assess the significance of EHD for a range of particle loadings.

II. LINEAR STABILITY OF THE UPPER TROPOSPHERE

A. Governing equations

In this work, the fluid dynamics in the troposphere is modeled according to the incompressible Navier-Stokes equations, given by

$$\frac{\partial \boldsymbol{u}}{\partial t} + \boldsymbol{u}\cdot\nabla\boldsymbol{u} = -\frac{1}{\rho}\nabla p + \nu\nabla^2\boldsymbol{u} + \frac{1}{\rho}\boldsymbol{F}_e - \Gamma z\frac{\partial \boldsymbol{u}}{\partial x} - \Gamma w\boldsymbol{e}_x, \tag{1}$$

where ρ is the gas-phase density, $\boldsymbol{u} = [u\ v\ w]^\mathsf{T}$ is the velocity, p is pressure, ν is the kinematic viscosity, and $\boldsymbol{F}_e$ is an EHD body force. The last two terms on the right-hand side of Eq. (1) are introduced to account for mean velocity gradients due to wind shear, where Γ is the shear rate, z is the vertical position, and $\boldsymbol{e}_x$ is the unit vector in the streamwise direction.

Within the upper troposphere, the electric permittivity is close to the vacuum permittivity ($\epsilon \approx \epsilon_0 = 8.854 \times 10^{-12}$ F/m) and can be assumed constant. As a consequence, the EHD body force can be expressed as $\boldsymbol{F}_e = q_f\boldsymbol{E}$, where the electric field, $\boldsymbol{E} = -\nabla\phi$, is determined by solving a Poisson equation for the electric potential ϕ, given by

$$\nabla^2\phi = -(q_f + q_p)/\epsilon, \tag{2}$$

which accounts for both the effect of space charge density in the fluid, q_f, and charge density of aerosol droplets, q_p. In the remainder of this study, the terms aerosols, droplets, and particles will be used interchangeably. Within the first 20 km of the troposphere, there exists a vertical gradient in air conductivity that gives rise to finite space charge density [33,34], even under fair weather conditions

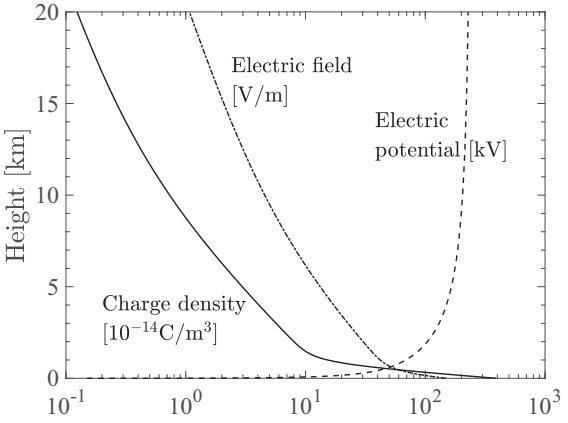

FIG. 1. Fair weather atmospheric conditions [37] used to define the background state in the stability analysis.

(see Fig. 1). We model the transport of space charge as

$$\frac{\partial q_f}{\partial t} + \nabla \cdot (\mu_I q_f \boldsymbol{E} - D_I \nabla q_f + q_f \boldsymbol{u} + q_f \Gamma z \boldsymbol{e}_x) = 0, \tag{3}$$

where $\mu_I \approx 10^{-4}$ m^2 V^{-1} s^{-1} is the ion mobility at 6 km altitude based on balloon-borne measurements [35] and $D_I = \mu_I k_B T/e$ is the molecular diffusion coefficient based on the Einstein relation [36]. Here k_B is the Boltzmann constant, T is temperature, and $e = 1.6 \times 10^{-19}$ C is the elementary charge. Within the first few kilometers of the atmosphere $D_I \approx 2 \times 10^{-6}$ m^2 s^{-1}.

B. Linear stability analysis

The flow quantities q_f, ϕ, p, $\boldsymbol{u}$, and $\boldsymbol{E}$ can be decomposed into a base state and a fluctuating component as $A = \overline{A} + A'$, where

$$A' = A_0(z) \exp(i\kappa_x x + i\kappa_y y) \exp(\omega\tau), \tag{4}$$

with A_0 the fluctuation amplitude, κ_x and κ_y the horizontal wave numbers, ω the growth rate, and $\tau = (\mu_I \overline{\phi}\, t)/L^2$ the timescale normalized over a vertical span L. Linearizing (1)–(3) and enforcing $\nabla \cdot \boldsymbol{u} = 0$, the following set of ODEs of total order 7 can be obtained to find solutions for the nondimensional fluctuation amplitudes of vertical velocity, $f(z) = w_0(z)L/[\mu_I \overline{\phi}(z)]$, and potential, $g(z) = \phi_0(z)/\overline{\phi}(z)$, according to

$$\left[\frac{\omega}{\mathrm{Pr}} - (D^2 - \alpha^2)\right](D^2 - \alpha^2) f = -R\frac{d\overline{q}_f}{dz}\frac{L^3}{\epsilon\overline{\phi}}\alpha^2 g - R\frac{\overline{E}L}{\overline{\phi}}(D^2 - \alpha^2)\alpha^2 g - S\hat{z}\beta(D^2 - \alpha^2)f - 2S\beta D f. \tag{5}$$

$$-\frac{\epsilon\overline{E}}{L^2}(D^2 - \alpha^2)Dg + \frac{d\overline{q}_f}{dz}Dg + \frac{\epsilon\overline{\phi}}{L^3}\omega(D^2 - \alpha^2)g + \frac{2\overline{q}_f}{L}(D^2 - \alpha^2)g = \frac{d\overline{q}_f}{dz}f. \tag{6}$$

Here $\hat{z} = z/L$, $\beta = L\, d/dx$, and $D = L\, d/dz$ are the normalized derivative operators, and $\alpha = L\sqrt{\kappa_x^2 + \kappa_y^2}$ is the normalized wave number. This analysis yields the following nondimensional numbers:

$$R = \frac{\epsilon\overline{\phi}}{\mu\mu_I}, \quad \mathrm{Pr} = \frac{\mu}{\rho\overline{\phi}\mu_I}, \quad S = \frac{\rho\Gamma L^2}{\mu}, \tag{7}$$

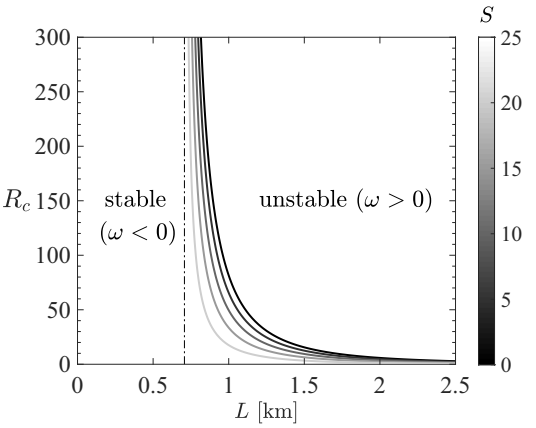

FIG. 2. Critical value of the electric Rayleigh number as a function of vertical span L for different shear Reynolds numbers S. The system is unconditionally stable when $L \leqslant 0.707$ km (denoted by the vertical dashed line).

which dictate stability and growth rate. Details on the derivation of the linearized equations and associated boundary conditions employed in the analysis are given in Appendix B, and a similar formulation can be found in Schneider and Watson [38] for a charged dielectric liquid film. R is sometimes referred to as the electric Rayleigh number [10] and represents the competition between turbulence production due to charge density fluctuations and dissipation due to viscosity. When R is greater than a critical value R_c, velocity fluctuations will increase with the Coulomb force, and below R_c the EHD-induced turbulence is damped by viscosity. Pr is the electric Prandtl number, a measure of electric timescale to the hydrodynamic timescale [38]. S is the shear Reynolds number that characterizes the importance of mean shear inertial forces to viscous forces over the vertical span L. Note that since $\bar{\phi}$ is also a function of L, all three nondimensional numbers are functions of L.

C. Effects of vertical span and shear rate

The ODEs reported in Sec. II B are solved numerically using a fourth-order Runge-Kutta scheme for a vertical thickness of the atmosphere $z_0 \leqslant z \leqslant z_0 + L$ with a base altitude $z_0 = 6$ km. We first consider base state values corresponding to fair weather conditions within the troposphere [37] (see Fig. 1). Figure 2 shows the minimum values of R_c such that the flow remains stable over all wave numbers, α, as a function of vertical span L. It can immediately be seen that the flow becomes more unstable as the vertical span increases. It is interesting to note that $R \approx 100$ in the troposphere, which corresponds to a vertical span of $L \approx 1$ km, consistent with typical cloud thicknesses observed at those elevations [39].

Wind shear is also known to play an important role in atmospheric dynamics and is responsible for Kelvin-Helmholtz instabilities that influence the turbulence energy budget [40]. Figure 2 shows that the system is unconditionally stable for $L \leqslant 0.707$ km regardless of wind shear, but for $L > 0.707$ km, R_c decreases with increasing shear rate, demonstrating shear acts to destabilize the flow, as expected. Even modest values of wind shear, i.e., $\Gamma > 1 \times 10^{-3}$ s^{-1}, will lead to values of S significantly larger than those considered in Fig. 2, affirming that atmospheric electricity (even in fair weather conditions) is a destabilizing mechanism in the troposphere. We note that the stability analysis neglects gravity, and thus these findings isolate the role of electric body forces on atmospheric stability.

Of key interest in the present study is the rate at which small disturbances in the velocity field grow due to EHD. The growth rate, ω, is obtained using prescribed values of α, R, and Pr. Using

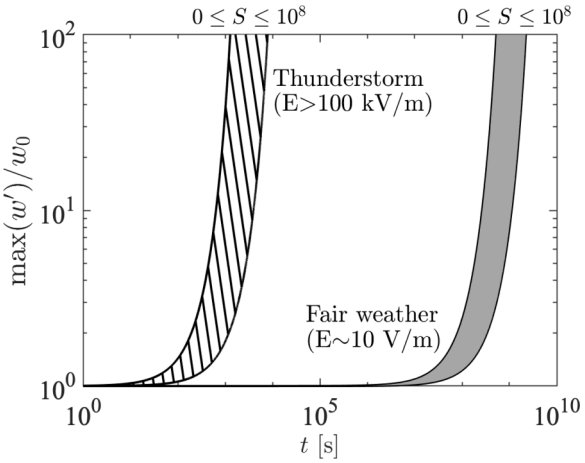

FIG. 3. Normalized growth of vertical velocity fluctuations under varying shear rates predicted by linear stability analysis under fair weather (solid fill) and thunderstorm (hatch fill) conditions.

typical fair weather conditions (Pr $\approx 2.5 \times 10^{-6}$), Fig. 3 shows that the maximum growth of vertical velocity fluctuations, w', by EHD is slow, taking approximately 10^9 s to amplify the fluctuations by two orders of magnitude. Using values relevant to thunderstorm conditions ($\overline{E} = 3 \times 10^5$ V/m and $\overline{\phi} = 2 \times 10^8$ V), similar growth is achieved in approximately 10^3 s. However, despite this enhanced growth rate, the timescales are still relatively slow, even as the shear rate varies by several orders of magnitude. It is important to note that the present linear stability analysis does not take into account detailed aerosol dynamics that are known to be significant in turbulent flows. Numerical simulations that explicitly take these dynamics into account will be presented in the following section.

III. NUMERICAL SIMULATIONS

A. Simulation configuration

Direct numerical simulations are performed to study the role of nonlinearities associated with aerosol dynamics not accounted for in the linear stability analysis. We consider charged particles suspended in homogeneous shear flow in the presence of a background electric field (see Fig. 4). The flow field and space charge are initialized using simple turning wave vectors referred to as Kelvin modes. These wave vectors are initially oriented as upstream waves that rotate as the flow is being sheared and transform into downstream waves. Kelvin modes are known to first experience a transient algebraic growth (a bypass transition) to turbulence and decay after they pass the turning point to downstream waves [41,42]. Nonlinear effects may couple with the initial transient growth leading to a "bootstrapping" mechanism [43]. If the electrostatic timescale is significantly smaller than the fluid timescale, heterogeneity in charge distribution may give rise to local EHD body forces during the transient period and prevent or postpone the fluid TKE from decaying.

We consider a triply periodic domain of length 0.256 m in each direction, discretized using 256^3 grid points. The maximum amount of charge each particle can carry is dictated by the Rayleigh limit, $Q_R = \pi\sqrt{8\epsilon\gamma d_p^3}$, where $\gamma = 0.0738$ N/m is the surface tension coefficient for water droplets and d_p is the particle diameter. The particle charge is taken to be $Q_p = \pm 0.1 Q_R$, and the average particle volume fraction varies between $0 \leqslant \Phi_v \leqslant 2 \times 10^{-3}$, corresponding to typical aerosol properties observed in thunderstorm conditions [37,44]. The root-mean-square EHD fluctuations, $(q_f E)_{\text{rms}} \equiv \sqrt{\langle (q_f E - \overline{q}_f \overline{E})^2 \rangle}$, is fixed as the particle loading varies, where angled brackets denote

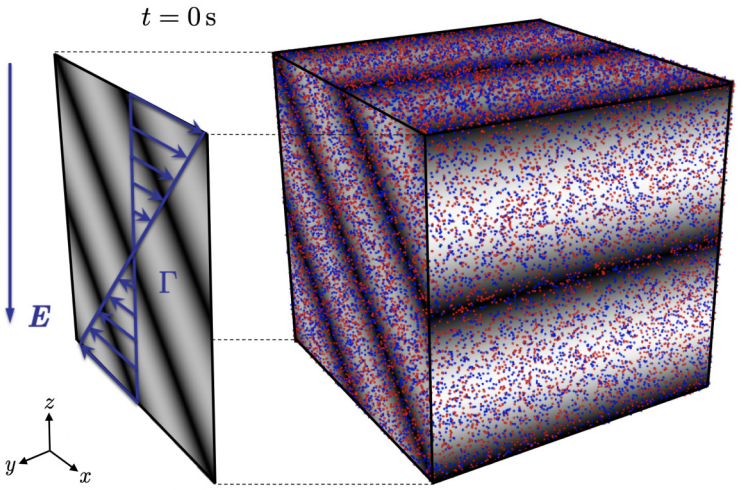

FIG. 4. Simulation configuration for $\Phi_v = 1 \times 10^{-4}$. Grayscale shows fluid velocity magnitude, ranging from 0 (black) to its maximum value (white). Particles are colored by charge: positive (red) and negative (blue).

a volume average. Given that $\overline{E}$ is constant and $\overline{q}_f = 0$, $(q_f E)_{\text{rms}} = \langle q_f^2 E'^2 \rangle$. Since the self-induced electric field E' is proportional to the local particle-phase charge density q_p, $(q_f E)_{\text{rms}} \sim \langle q_f^2 q_p^2 \rangle$ is held constant for each simulation. This is done to avoid a trivial solution (e.g., increasing the effect of EHD with increasing volume fraction) and isolate the effect of particle dynamics on TKE production. Therefore, as Φ_v increases, q_f decreases accordingly (see Table I).

B. Numerics

The fluid-phase equations (1)–(3) are solved on a staggered grid with second-order spatial accuracy for both the convective and viscous terms, and the second-order accurate semi-implicit Crank-Nicolson scheme is used for time advancement [45]. Periodic shear boundary conditions are enforced in the z direction using a discretely conservative algorithm recently proposed by Kasbaoui *et al.* [42]. Individual aerosol particles are tracked in a Lagrangian manner [46] governed by Newton's second law of motion

$$\frac{d\boldsymbol{x}_p^{(i)}}{dt} = \boldsymbol{v}_p^{(i)} \quad \text{and} \quad m_p \frac{d\boldsymbol{v}_p^{(i)}}{dt} = \boldsymbol{F}_{\text{drag}}^{(i)} + \boldsymbol{F}_c^{(i)}, \tag{8}$$

TABLE I. Parameters used in the homogeneous shear simulations. q_{f_0} is varied with Φ_v such that $(q_f E)_{\text{rms}} \sim \sqrt{\langle q_p^2 q_f^2 \rangle}$ is held constant. All simulations are performed with conditions of $d_p/\Delta x = 0.1$ and $\Gamma = 1.5$.

Φ_v	Mean volume fraction	0	1×10^{-4}	4×10^{-4}	1×10^{-3}	2×10^{-3}
N_p	Number of particles	0	3.2×10^6	1.3×10^7	3.2×10^7	6.4×10^7
q_{f_0} [C/m^3]	Space charge fluctuation	2×10^{-8}	1×10^{-8}	5×10^{-9}	3.2×10^{-9}	2.2×10^{-9}
d_p	Particle diameter			100 μm		
Q_p	Particle charge			$\pm 7.27 \times 10^{-13}$ C		
ρ_p/ρ_f	Density ratio			1000		
$\overline{E}$	Background electric field			3.0×10^5 V/m		

where $\boldsymbol{x}_p^{(i)}$ and $\boldsymbol{v}_p^{(i)}$ are the instantaneous position and velocity of particle "i," respectively, and m_p is its mass. The drag force is modeled according to the standard drag correlation of Schiller and Naumann [47] as

$$\boldsymbol{F}_{\text{drag}}^{(i)} = \frac{m_p}{\tau_p}\left(\boldsymbol{u}\left[\boldsymbol{x}_p^{(i)}\right] - \boldsymbol{v}_p^{(i)}\right)\left(1 + 0.15\text{Re}_p^{0.687}\right), \tag{9}$$

where $\boldsymbol{u}[\boldsymbol{x}_p^{(i)}]$ is the fluid velocity interpolated to the center position of the ith particle, $\text{Re}_p = |\boldsymbol{u}[\boldsymbol{x}_p^{(i)}] - \boldsymbol{v}_p^{(i)}|d_p/\nu$ is the particle Reynolds number, and $\tau_p = \rho_p d_p^2/(18\rho\nu)$ is the particle response time. The electrostatic force is given by

$$\boldsymbol{F}_c^{(i)} = Q_p^{(i)}\boldsymbol{E}\left[\boldsymbol{x}_p^{(i)}\right], \tag{10}$$

where $Q_p^{(i)}$ is the charge of the ith particle and $\boldsymbol{E}[\boldsymbol{x}_p^{(i)}]$ is the electric field at the particle position. The particle concentrations are low enough such that interparticle collisions and direct two-way coupling due to interphase momentum exchange can be neglected. Instead, aerosols affect the gas phase indirectly via their charge distribution.

The aerosol charge density, q_p, is obtained by projecting the particle charge to the Eulerian grid according to

$$q_p(\boldsymbol{x}, t) = \sum_{i=1}^{N_p} Q_p^{(i)}\mathcal{W}\left[\boldsymbol{x} - \boldsymbol{x}_p^{(i)}(t)\right], \tag{11}$$

where $\mathcal{W}$ is a second-order accurate polynomial weighting function and N_p is the number of particles. A second-order Runge-Kutta scheme is used for updating each particle's position and velocity. Further details about the numerical implementation can be found in Yao and Capecelatro [15].

Because the simulation domain is periodic, q_f and $\boldsymbol{E}$ must be decomposed into mean and fluctuating components and only q_f' and $\boldsymbol{E}'$ are solved for. Equation (2) can be rewritten as $\nabla^2\phi' = -(q_f' + q_p)/\epsilon$, and the electric field fluctuation can be solved via $\boldsymbol{E}' = -\nabla\phi'$. We note that particles are assigned equal and opposite charge such that $\langle q_p\rangle = 0$ and the Poisson equation is well posed. The total electric field is then reconstructed as $\boldsymbol{E} = \boldsymbol{E}' + \overline{\boldsymbol{E}}$, and similarly $q_f = q_f' + \overline{q}_f$, with $\overline{\boldsymbol{E}} = [0\,0\,\overline{E}]^\mathsf{T}$. In each simulation, $\overline{q}_f = 0$ and the amplitude of q_f' is prescribed as q_{f0}. Parameters are chosen to correspond to thunderstorm conditions at an altitude of 6 km as summarized in Table I.

C. Evolution and growth of TKE

The aerosol droplets are initially randomly distributed throughout the domain. As shown in Fig. 5, horizontal wind shear combined with the background electric field leads to the onset of particle clustering in high-strain regions, which eventually generates fluctuations in fluid velocity via coupling with the charge density. Particle clustering arises from a similar mechanism identified by Kasbaoui *et al.* [32], except here the body force is due to the electric field instead of gravity, and the momentum coupling exists through the charge density instead of the drag force. In the absence of charged droplets, the initial Kelvin modes are rotated and decay without introducing any fluctuations. Gas-phase velocity fluctuations become more intense with increasing droplet loading. To identify the mechanisms responsible for this, we evaluate the evolution of Reynolds stresses, governed by

$$\frac{d\langle u_i'u_j'\rangle}{dt} = \mathcal{P}_{ij} + \mathcal{R}_{ij} - \varepsilon_{ij} + \mathcal{E}_{ij}, \tag{12}$$

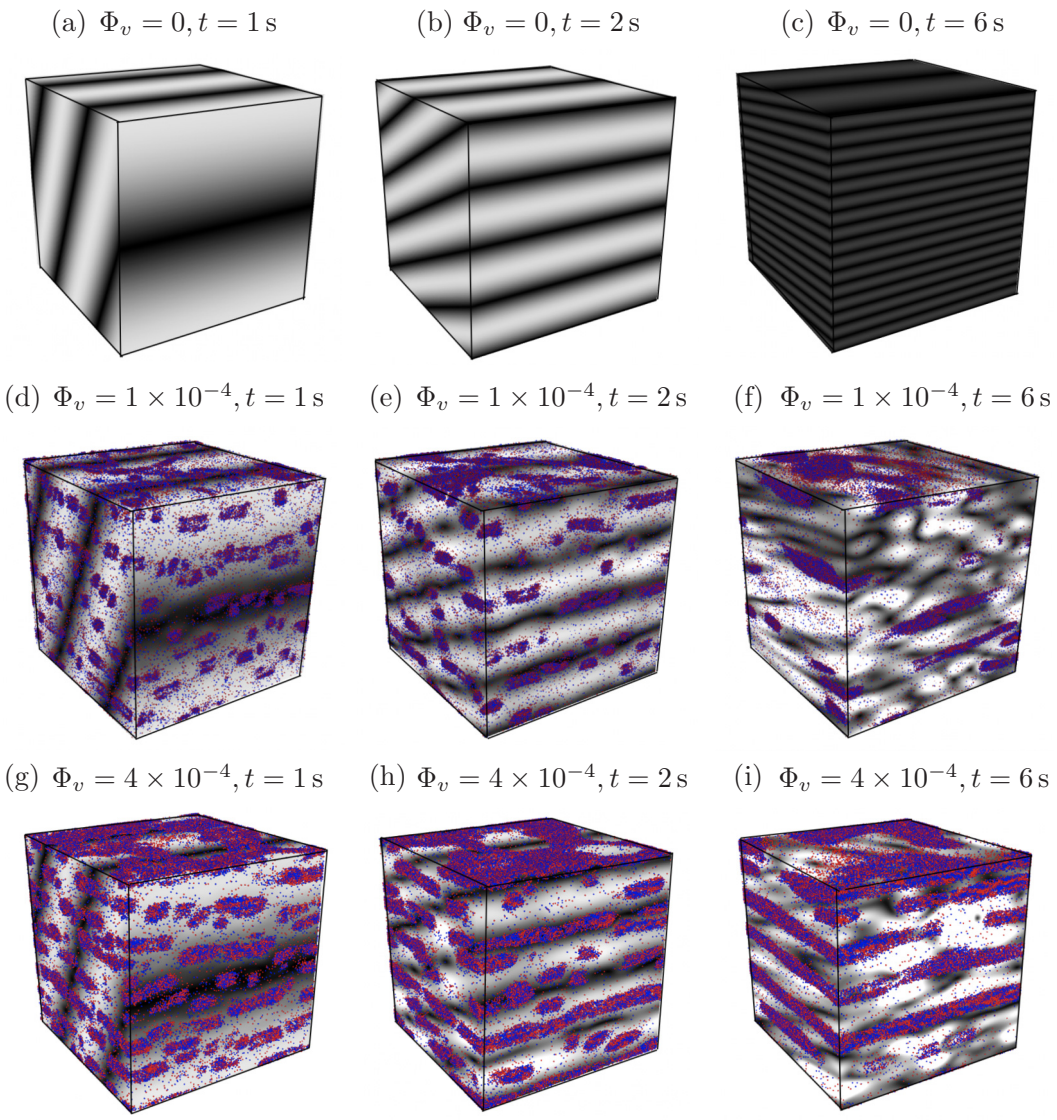

FIG. 5. Temporal evolution of the gas and particle phases with volume fraction increasing from top to bottom and time increasing from left to right. Color scheme same as Fig. 4.

where $\mathcal{P}_{ij}$, $\mathcal{R}_{ij}$, and ε_{ij} denote mean-gradient production, pressure strain, and viscous dissipation, respectively [48], given by

$$\mathcal{P}_{ij} \equiv -\langle u_i' u_k' \rangle \frac{\partial \langle u_j \rangle}{\partial x_k} - \langle u_j' u_k' \rangle \frac{\partial \langle u_i \rangle}{\partial x_k}, \tag{13}$$

$$\mathcal{R}_{ij} \equiv \left\langle \frac{p'}{\rho} \left(\frac{\partial u_i'}{\partial x_j} + \frac{\partial u_j'}{\partial x_i} \right) \right\rangle, \tag{14}$$

$$\varepsilon_{ij} \equiv 2\nu \left\langle \frac{\partial u_i'}{\partial x_k} \frac{\partial u_j'}{\partial x_k} \right\rangle \tag{15}$$

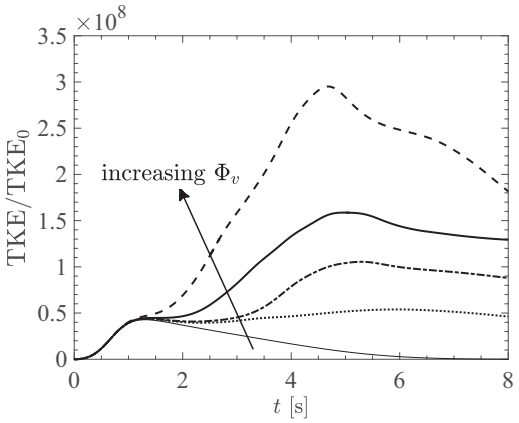

FIG. 6. Normalized TKE evolution for particle loading $\Phi_v = 0$ (–), 1×10^{-4} ($\cdots$), 4×10^{-4} (– -), 1×10^{-3} (–), and 2×10^{-3} (- -).

and

$$\rho \mathcal{E}_{ij} = \langle E_j \rangle \langle q'_f u'_i \rangle + \langle E_i \rangle \langle q'_f u'_j \rangle + \langle q'_f E'_j u'_i \rangle + \langle q'_f E'_i u'_j \rangle \tag{16}$$

are contributions from EHD. In the present configuration, $\langle E_1 \rangle = \langle E_2 \rangle = 0$ and $\langle E_3 \rangle = \overline{E}$. Also note the last two terms on the right-hand side of Eq. (16) containing triple correlations were found to be negligible compared to the first two terms. Taking one-half the trace of (12) yields a transport equation for the TKE, defined as $\langle u'_i u'_i \rangle / 2$ (repeated indices imply summation). The contributions from EHD, $\mathcal{E}_{ii}/2$, contain two terms. $\mathcal{E}_P = \overline{E} \langle q'_f w' \rangle / \rho$ represents production due to the background electric field and correlation between charge density and vertical velocity fluctuations. The second contribution, $\mathcal{E}_T = \langle q'_f E'_i u'_i \rangle / \rho$ is found to be negligible in the present study.

The temporal evolution of TKE is shown in Fig. 6. All cases exhibit similar algebraic growth at early times. An analytic solution for this early time behavior is provided in Appendix A, which is shown to independent of the aerosol distribution. It can immediately be seen that increasing particle loading enhances TKE after the initial algebraic growth ($t \gtrapprox 1$ s). By transferring the charge density from the carrier phase to aerosol particles, the TKE is amplified by as much as a factor of 6 for the highest loading under consideration. It should be noted that the size of the simulation domain is constrained by the high computational cost in tracking $O(10^8)$ individual particles. Based on the linear stability analysis performed in Sec. II C, larger domain sizes should result in greater enhancement of TKE. Moreover, a scaling analysis by Di Renzo and Urzay [14] demonstrated that while clustering occurs at the microscale (at the same scale as the smallest turbulent eddies), the self-induced electric field can span much larger scales. Thus, the effects reported here are anticipated to be greater under more relevant length scales.

D. Reynolds stress budget

After the initial algebraic growth is complete, turbulence modulation by charged aerosols is apparent. The temporal evolution of Reynolds stresses is shown in Fig. 7. When aerosol particles are absent ($\Phi_v = 0$), the vertical component of Reynolds stress, $\langle w'w' \rangle$, initially grows due to production by EHD ($\mathcal{E}_{33} = 2\overline{E} \langle q'_f w' \rangle / \rho$). This term then contributes to mean-gradient production ($\mathcal{P}_{13} = -\langle w'w' \rangle \Gamma$) that increases $\langle u'w' \rangle$. Next, the energy is transferred to the streamwise component $\langle u'u' \rangle$. Because there is no mechanism to sustain TKE when charged aerosol droplets are absent, all three components decay to zero at late times due to viscous dissipation, as shown in Fig. 6. When charged droplets are introduced, the Reynolds stresses follow a similar trend at early times and deviate at later times. Only the vertical component $\langle w'w' \rangle$ approaches

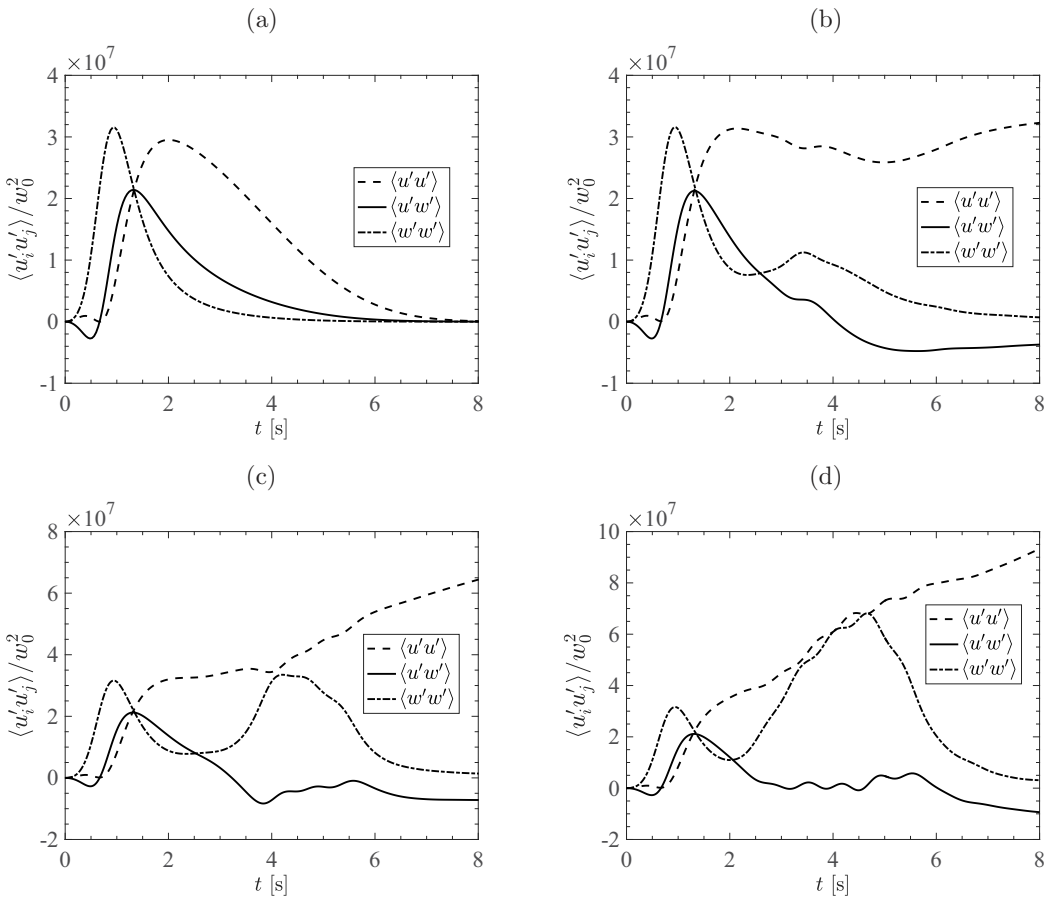

FIG. 7. Evolution of the Reynolds stresses normalized by w_0^2 for (a) $\Phi_v = 0$, (b) 1×10^{-4}, (c) 4×10^{-4}, and (d) 1×10^{-3}.

zero, while $\langle u'w' \rangle$ levels off to a negative value, and the streamwise component, $\langle u'u' \rangle$, is seen to increase. This effect is enhanced with increasing particle volume fraction as shown in Figs. 7(b)–7(d).

The Reynolds stress budgets are reported for $\Phi_v = 1 \times 10^{-4}$ in Fig. 8 to further understand how energy is transferred between the separate components. We note that the trends reported here are consistent at other values of Φ_v. The initial sinusoidal fluctuation in space charge and vertical velocity together with the background electric field generate a nonzero EHD source $\mathcal{E}_{33} = 2\overline{E}\langle q_f' w' \rangle / \rho$. As a result, the vertical component of Reynolds stress, $\langle w'w' \rangle$, grows due to this production terms [see Fig. 8(a)]. A significant portion of this energy is also transferred to the corresponding pressure strain, $\mathcal{R}_{33} = \langle\, 2p'(\partial w'/\partial z)/\rho \,\rangle$, and consequently $\langle w'w' \rangle$ decays to zero at late times.

The EHD production term, $\mathcal{E}_{33}$, then decays as a result of diffusion of space charge, at which time pressure strain, $\mathcal{R}_{13} = \langle\, p'(\partial u'/\partial z + \partial w'/\partial x)/\rho \,\rangle$, acts to redistribute the energy to $\langle u'w' \rangle$. Figure 8(b) reveals that while the streamwise velocity fluctuations increase, a new EHD source term, $\mathcal{E}_{13} = \overline{E}\langle q_f' u' \rangle / \rho$, emerges, further augmenting $\langle u'w' \rangle$. At late time, pressure strain continues to transfer energy from $\langle u'w' \rangle$, similar to $\langle w'w' \rangle$, and the corresponding mean-gradient production, $\mathcal{P}_{13} = -\langle w'w' \rangle \Gamma$, is negative and acts as a sink of $\langle u'w' \rangle$. As a result, $\langle u'w' \rangle$ eventually decays and approaches a negative value when production and dissipation balance.

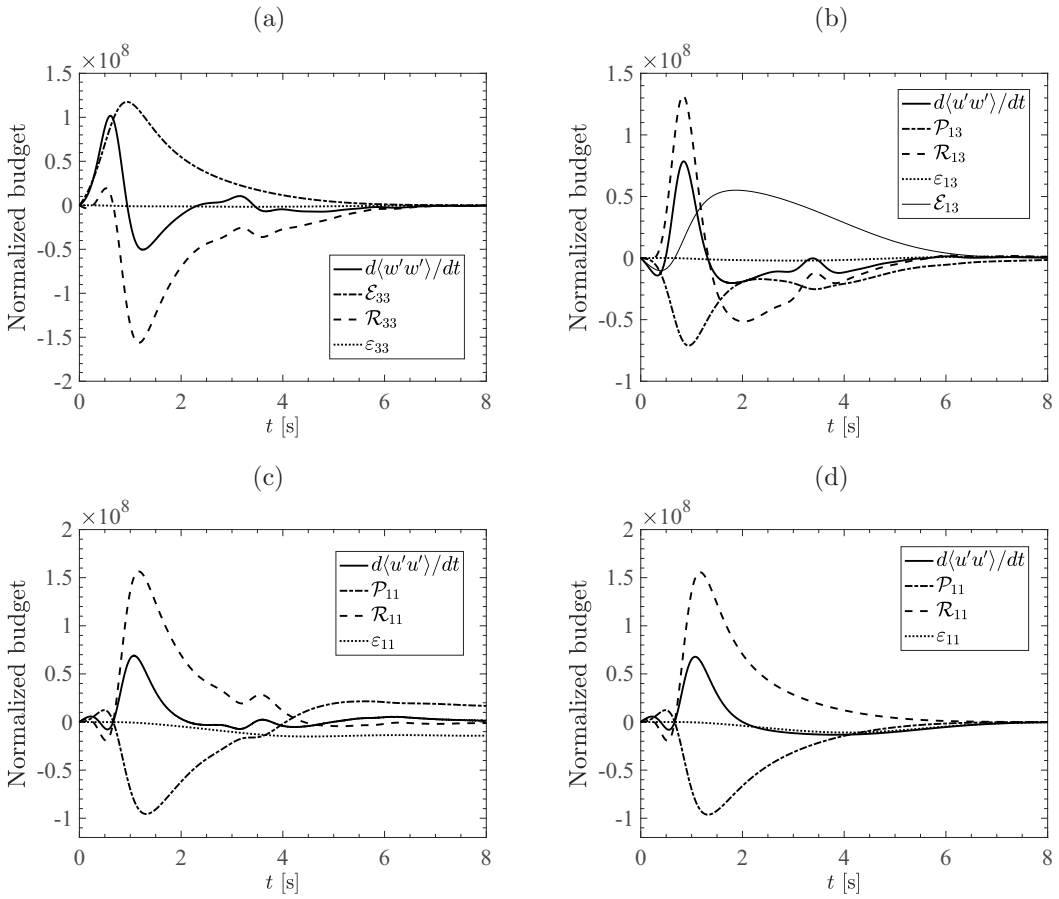

FIG. 8. Budget of (a) $\langle w'w' \rangle$, (b) $\langle u'w' \rangle$, and (c) $\langle u'u' \rangle$ normalized by Γw_0^2 for $\Phi_v = 1 \times 10^{-4}$. (d) $\langle u'u' \rangle$ normalized by Γw_0^2 in the absence of particles.

Figure 8(c) shows the budget for the streamwise component of the Reynolds stress, $\langle u'u' \rangle$. As energy is transferred to the streamwise components, $\langle u'u' \rangle$ is first augmented by the corresponding pressure strain, $\mathcal{R}_{11} = \langle 2p'(\partial u'/\partial x)/\rho \rangle$, during the early stage, then mean-gradient production, $\mathcal{P}_{11} = -2\langle u'w' \rangle \Gamma$, acts as a source when $\langle u'w' \rangle$ reaches a negative equilibrium that later sustains $\langle u'u' \rangle$. Note that unlike the other two components of Reynolds stress, the streamwise component always has nonzero production and therefore continues to increase even at late time. Comparing Figs. 8(c) and 8(d), it can be seen that this nonzero equilibrium state of production ($\mathcal{P}_{11}$) occurs only when charged aerosols are present.

A schematic summarizing the energy transfer is illustrated in Fig. 9. As depicted by the solid lines, a background electric field combined with fluctuations in velocity and space charge yields production of TKE that is eventually dissipated into heat. In the absence of charged droplets, no other mechanism exists to further produce TKE. However, when aerosol droplets are present, turbulence can be sustained through two additional processes: (1) turbulence preferentially concentrates charged particles, resulting in fluctuations in electric potential that self-induces an electric field, enhancing $\mathcal{E}_{33}$ and TKE, and (2) the space charge fluctuation induced by the electric field contributes to another EHD source term, $\mathcal{E}_{13}$, which enhances $\langle u'w' \rangle$, contributing to mean-gradient production ($\mathcal{P}_{11}$) that further augments TKE. This three-way coupling gives rise to a feedback loop that enhances TKE beyond the initial algebraic growth.

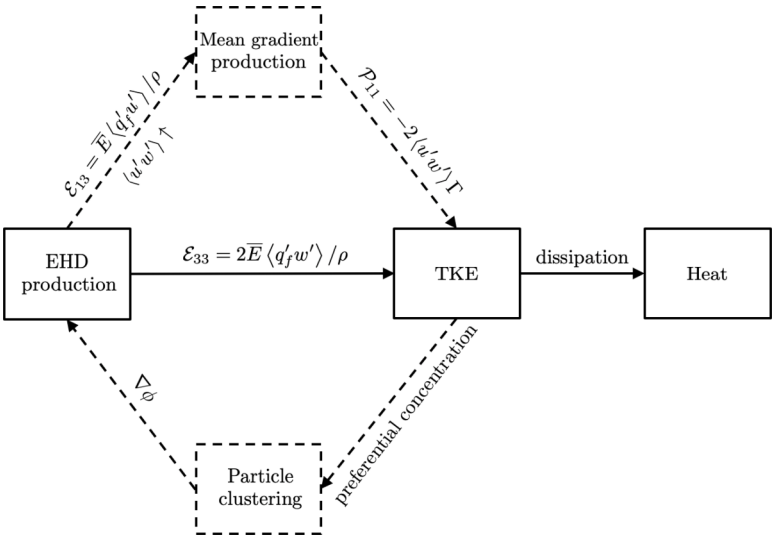

FIG. 9. Energy transfer due to three-way coupling between turbulence, charged particles, and a background electric field. The dashed lines represent energy transfer when aerosol particles are present. Fluctuations in vertical velocity and space charge give rise to an EHD source term, $\mathcal{E}_{33}$, that produces TKE. In the absence of charged aerosol particles, TKE is eventually dissipated to heat. When particles are present, preferential concentration by the turbulence generates inhomogeneities in particle distribution and consequently gradients in electric potential. This further contributes to the EHD source term $\mathcal{E}_{33}$ in addition to $\mathcal{E}_{13}$ that generates TKE via mean gradient production.

IV. CONCLUSION

We presented a theoretical and numerical study on the electrohydrodynamic generation of atmospheric turbulence under fair weather and thunderstorm conditions. The focus of this study was on the three-way coupling between turbulence, charged aerosol droplets, and a background electric field. A canonical flow configuration was presented to simulate the upper troposphere, in which a random distribution of charged particles was placed in homogeneous shear flow with a uniform electric field.

Linear stability analysis was performed using base state parameters relevant to fair weather conditions in the upper troposphere. Atmospheric stability was characterized by the electric Rayleigh number, which was found to be a function of vertical span and shear rate. The stability analysis revealed that the atmospheric fluid dynamics are most unstable over a vertical span consistent with typical cloud thicknesses observed at these elevations. The growth rate in velocity fluctuations was estimated using both fair weather and thunderstorm parameters, which was found to be slow even under thunderstorm conditions.

Direct numerical simulations revealed a nonlinear feedback mechanism that acts to accelerate turbulence production under thunderstorm conditions. It was found that horizontal wind shear combined with EHD body forces led to the onset of particle clustering that generated fluctuations in charge density. These fluctuations acted to augment turbulent kinetic energy (TKE) after the initial algebraic growth. TKE was initially produced in the vertical direction and was later transferred to the streamwise (shear) components. The streamwise velocity gradients acted to induce fluctuations in aerosol concentration and consequently generated gradients in electric potential, resulting in an increase in the EHD body force and the process repeated. TKE was enhanced by up to a factor of six as the particle loading increased.

The present numerical and theoretical analysis demonstrated that charged aerosols in the atmosphere can couple nonlinearly with the background electric field to enhance the onset of TKE.

It is important to note that other effects may be at play as well. Particles are capable of transferring charge among each other or acquire charge through triboelectric effects [49–52]. In addition, the droplet size may vary due to evaporation and condensation. Additional instabilities may also arise when gravity is present, which may add to the TKE augmentation studied here. In the present study, we isolate the effect of charged aerosols on turbulence generation, and therefore these effects were not included. However, the Eulerian-Lagrangian simulation framework can be extended to account for these kinetic processes in TKE augmentation in future work.

ACKNOWLEDGMENTS

The authors wish to thank Dr. Houssem Kasbaoui for valuable discussions and providing the homogeneous shear code. The computing resources and assistance provided by the staff of Advanced Research Computing at the University of Michigan, Ann Arbor, is greatly appreciated. This work was supported in part by the Office of Naval Research (ONR) Award Number N00014-19-1-2202.

APPENDIX A: ANALYTICAL SOLUTION OF THE INITIAL ALGEBRAIC GROWTH

In homogeneous shear flows, the initial algebraic growth is known to sustain large amplification of perturbation energy that may introduce nonlinear effects and lead to onset of turbulence [53–57]. Because conventional linear stability analysis fails to accurately predict the transient growth, other techniques, such as non-normal modal analysis [43,58,59] or the Wentzel-Kramers-Brillouin (WKB) method [60,61], have been used. In the present analysis, we consider the method of characteristics. By neglecting the particle phase, Eqs. (1) and (3) are rewritten along characteristics in Fourier space, together with the wave vector characteristic equations, resulting in the following three coupled ODEs:

$$\begin{aligned}
\frac{d\boldsymbol{\kappa}}{dt} &= -\boldsymbol{\nabla}\mathbf{u}_b^T \cdot \boldsymbol{\kappa}, \\
\frac{d\hat{q}_f}{dt} &= -i\mu_I \overline{E}\kappa_3 \hat{q}_f - D_I \kappa^2 \hat{q}_f, \\
\frac{d\hat{w}}{dt} &= \frac{2\Gamma\kappa_1\kappa_3}{\kappa^2}\hat{w} - \nu\kappa^2\hat{w} + \left(1 - \frac{\kappa_3^2}{\kappa^2}\right)\frac{\hat{q}_f\overline{E}}{\rho},
\end{aligned} \tag{A1}$$

where the hat denotes the Fourier transform of a quantity, $\boldsymbol{\kappa} = [\kappa_1\, \kappa_2\, \kappa_3]^\mathsf{T}$ is the wave vector, and $\boldsymbol{\nabla}\mathbf{u}_b = \Gamma \mathbf{e}_1\mathbf{e}_3^\mathsf{T}$ is the base state velocity gradient tensor. The vertical velocity can be determined by assuming $w'(t, \boldsymbol{x}) = \hat{w}(t)\exp[i\boldsymbol{\kappa}(t)\cdot\boldsymbol{x}]$. The remaining velocity components can be obtained by enforcing continuity. As shown in Fig. 10, the second-order algebraic growth closely matches the numerical simulations from Sec. III, confirming that charged aerosols do not affect the initial algebraic growth rate.

The second-order algebraic initial growth rate can be approximated analytically from Eq. (A1). Solving the wave vector characteristic equation yields $\kappa_1 = \kappa_0 = 2\pi/L$ and $\kappa_3 = (1 - \Gamma t)\,\kappa_0$. With this, the magnitude of $\hat{q}_f$ can easily be obtained by solving the first-order linear ODE in Eq. (A1):

$$\hat{q}_f(t) = \hat{q}_{f0}\exp\left[-\tfrac{1}{3}D_I\kappa_0^2 t(\Gamma^2 t^2 - 3\Gamma t + 6)\right]. \tag{A2}$$

Solving $\hat{q}_f$, the third ODE for velocity results in a first-order linear equation and can be approximated via a Taylor series expansion according to

$$\begin{aligned}
\frac{d\hat{w}}{dt} &= \frac{1}{1 + (1 - \Gamma t)^2}\frac{\hat{q}_{f0}\overline{E}}{\rho}\exp\left[-\frac{1}{3}D_I\kappa_0^2 t(\Gamma^2 t^2 - 3\Gamma t + 6)\right] \\
&\approx \frac{1}{1 + (1 - \Gamma t)^2}\frac{\hat{q}_{f0}\overline{E}}{\rho}\left[1 - 2D_I\kappa_0^2\, t + D_I\kappa_0^2\left(\Gamma + 2D_I\kappa_0^2\right)t^2\right].
\end{aligned} \tag{A3}$$

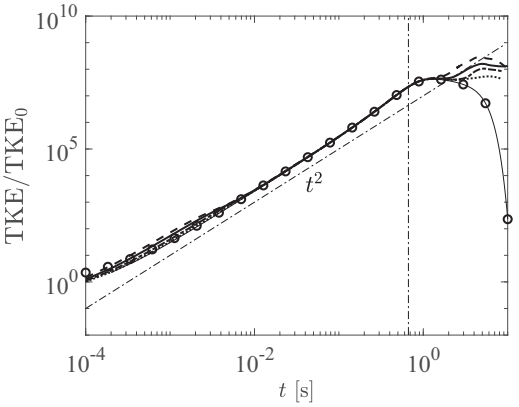

FIG. 10. Normalized TKE evolution for particle loading $\Phi_v = 0$ (–), 1×10^{-4} ($\cdots$), 4×10^{-4} (– -), 1×10^{-3} (–), and 2×10^{-3} (- -). Theoretical solution obtained from Eq. (A1) ($\circ$) is shown for comparison. The vertical dashed line indicates the turning point from upstream and downstream waves.

The first two terms on the right-hand-side can be neglected since they are orders of magnitude smaller than the last term. Integrating Eq. (A3) yields

$$\begin{aligned}\hat{w}(t) &= \hat{w}_0 - \frac{\hat{q}_{f0}\overline{E}}{\rho\Gamma^2}\left(\Gamma - 2D_I\kappa_0^2\right)\left[\tan^{-1}(1-\Gamma t) - \frac{\pi}{4}\right] \\ &\approx \hat{w}_0 + \frac{\hat{q}_{f0}\overline{E}}{2\rho\Gamma}\left(\Gamma - 2D_I\kappa_0^2\right)t. \end{aligned} \tag{A4}$$

By applying continuity, the streamwise velocity can be expressed as

$$\hat{u}(t) = -\frac{\hat{w}(t)\kappa_3}{\kappa_1} = -\hat{w}_0(1-\Gamma t) - \frac{\hat{q}_{f0}\overline{E}}{2\rho\Gamma}\left(\Gamma - 2D_I\kappa_0^2\right)(1-\Gamma t)t. \tag{A5}$$

With this, the TKE can be approximated by

$$\mathrm{TKE}(t) = \frac{1}{2}(\hat{w}^2 + \hat{u}^2) \approx \mathrm{TKE}_0 + \frac{\hat{q}_{f0}^2\overline{E}^2}{2\rho^2\Gamma^2}\left(\Gamma - 2D_I\kappa_0^2\right)^2 t^2 = O(t^2), \tag{A6}$$

which implies when t is small, the initial growth of TKE is second order. This growth rate is also consistent with the well-known quadratic-scaling law for the transient energy growth in uniform shear flow [57,62].

APPENDIX B: LINEARIZATION AND NONDIMENSIONALIZATION OF THE GOVERNING EQUATIONS

We start with the governing equations (1) and (3) and neglect the convective term in the momentum equation and diffusion term in the charge transport equation due to their relatively small magnitudes:

$$\left(\rho\frac{\partial}{\partial t} - \mu\nabla^2\right)\boldsymbol{u} = q_f\boldsymbol{E} - \nabla p - \rho\Gamma z\frac{\partial \boldsymbol{u}}{\partial x} - \rho\Gamma w\boldsymbol{e}_x, \tag{B1}$$

$$\frac{\partial q_f}{\partial t} + \nabla\cdot(\mu_I q_f\boldsymbol{E} + q_f\boldsymbol{u} + q_f\Gamma z\boldsymbol{e}_x) = 0. \tag{B2}$$

The flow quantities q_f, ϕ, p, $\boldsymbol{u}$, and $\boldsymbol{E}$ are decomposed into a base state and a fluctuating component as $A = \overline{A} + A'$, where

$$A' = A_0(z)\exp(i\kappa_x x + i\kappa_y y)\exp(\omega\tau), \tag{B3}$$

with A_0 the fluctuation amplitude, κ_x and κ_y the horizontal wave numbers, ω the growth rate, and $\tau = (\mu_I\overline{\phi}\,t)/L^2$ the timescale normalized over a vertical span L. Consider (B1) first at a base case where $\overline{\boldsymbol{u}} = [\overline{u}\,\overline{v}\,\overline{w}]^{\mathsf{T}} = 0$, then (B1) reduces to

$$\overline{q}_f\overline{\boldsymbol{E}} = \boldsymbol{\nabla}\overline{p}, \tag{B4}$$

and by subtracting (B1) by (B4), we have

$$\left(\rho\frac{\partial}{\partial t} - \mu\nabla^2\right)\boldsymbol{u} = (q_f\boldsymbol{E})' - \nabla p' - \rho\Gamma z\frac{\partial \boldsymbol{u}}{\partial x} - \rho\Gamma w\boldsymbol{e}_x, \tag{B5}$$

then for incompressible flow, we can take divergence of (B5) and apply $\boldsymbol{\nabla}\cdot\boldsymbol{u} = 0$ to arrive at

$$\nabla^2 p' = \boldsymbol{\nabla}\cdot(q_f\boldsymbol{E})'. \tag{B6}$$

Now consider the vertical component of (B5),

$$\left(\rho\frac{\partial}{\partial t} - \mu\nabla^2\right)w' = (q_f E_3)' - \frac{\partial}{\partial z}p' - \rho\Gamma z\frac{\partial w'}{\partial x}, \tag{B7}$$

where we can take the Laplacian of (B7) and incorporate (B6)

$$\left(\rho\frac{\partial}{\partial t} - \mu\nabla^2\right)\nabla^2 w' = \nabla^2(q_f E_3)' - \frac{\partial}{\partial z}[\boldsymbol{\nabla}\cdot(q_f\boldsymbol{E})'] - \rho\Gamma\nabla^2\left(z\frac{\partial w'}{\partial x}\right), \tag{B8}$$

where

$$\begin{aligned}\frac{\partial}{\partial z}[\boldsymbol{\nabla}\cdot(q_f\boldsymbol{E})'] &= \frac{\partial}{\partial z}[\boldsymbol{\nabla}\cdot(q_f{}'\overline{\boldsymbol{E}}) + \boldsymbol{\nabla}\cdot(\overline{q}_f\boldsymbol{E}')] \\ &= \overline{E}\,\frac{\partial^2 q_f'}{\partial z^2} + \frac{d^2\overline{q}_f}{dz^2}E_3' + \frac{d\overline{q}_f}{dz}\frac{\partial E_3'}{\partial z} + 2\,\frac{q_f'}{\epsilon}\frac{d\overline{q}_f}{dz} + 3\,\frac{\overline{q}_f}{\epsilon}\frac{\partial q_f'}{\partial z},\end{aligned} \tag{B9}$$

$$\begin{aligned}\nabla^2(q_f E_3)' &= \nabla^2(q_f'\overline{E}) + \nabla^2(\overline{q}_f E_3') \\ &= \overline{E}\,\nabla^2 q_f' + \frac{q_f'}{\epsilon}\frac{d\overline{q}_f}{dz} + 2\,\frac{dq_f'}{dz}\frac{d\overline{E}}{dz} + \overline{q}_f\nabla^2 E_3' + E_3'\frac{d^2\overline{q}_f}{dz^2} + 2\,\frac{d\overline{q}_f}{dz}\frac{dE_3'}{dz},\end{aligned} \tag{B10}$$

and

$$\rho\Gamma\nabla^2\left(z\frac{\partial w'}{\partial x}\right) = \rho\Gamma z\frac{\partial}{\partial x}(\nabla^2 w') + 2\rho\Gamma\frac{\partial}{\partial x}\left(\frac{\partial w'}{\partial z}\right). \tag{B11}$$

Combining (B8)–(B11) gives

$$\begin{aligned}\left(\rho\frac{\partial}{\partial t} - \mu\nabla^2\right)\nabla^2 w' = {} & \frac{\partial^2 q_f'}{\partial z^2}\overline{E} - \frac{q_f'}{\epsilon}\frac{d\overline{q}_f}{dz} + \frac{\overline{q}_f}{\epsilon}\frac{\partial q_f'}{\partial z} + \overline{q}_f\nabla^2 E_3' + \frac{d\overline{q}_f}{dz}\frac{\partial E_3'}{\partial z} + \overline{E}\nabla^2 q_f' \\ & - \rho\Gamma z\frac{\partial}{\partial x}(\nabla^2 w') - 2\rho\Gamma\frac{\partial}{\partial x}\left(\frac{\partial w'}{\partial z}\right).\end{aligned} \tag{B12}$$

Using $q_f' = -\epsilon\nabla^2\phi'$ and $E_3' = -d\phi'/dz$, (B12) can be rewritten in terms of potential

$$\left(\rho\frac{\partial}{\partial t} - \mu\nabla^2\right)\nabla^2 w' = \epsilon\overline{E}\nabla^2\nabla_1^2\phi' + \frac{d\overline{q}_f}{dz}\nabla_1^2\phi' - \rho\Gamma z\frac{\partial}{\partial x}(\nabla^2 w') - 2\rho\Gamma\frac{\partial}{\partial x}\left(\frac{\partial w'}{\partial z}\right), \tag{B13}$$

where $\nabla_1^2 = \partial^2/\partial x^2 + \partial^2/\partial y^2$. Similarly (B2) can be linearized the same way in the vertical direction to obtain

$$-\epsilon\bar{E}\frac{\partial}{\partial z}\nabla^2\phi' + \frac{d\bar{q}_f}{dz}\frac{\partial\phi'}{\partial z} + \frac{\epsilon}{\mu_I}\frac{\partial}{\partial t}\nabla^2\phi' + 2\bar{q}_f\nabla^2\phi' = \frac{1}{\mu_I}\frac{d\bar{q}_f}{dz}w'. \tag{B14}$$

Recall that $\phi' = \phi_0(z)\exp(i\kappa_x x + i\kappa_y y)\exp(\omega\tau)$ and $w' = w_0(z)\exp(i\kappa_x x + i\kappa_y y)\exp(\omega\tau)$, so $\nabla^2\phi' = [-(\kappa_x^2+\kappa_y^2) + (d/dz)^2]\phi'$ and $\nabla^2 w' = [-(\kappa_x^2+\kappa_y^2) + (d/dz)^2]w'$; therefore the equations can be nondimensionalized with $\nabla^2 = (D^2-\alpha^2)/L^2$, $\nabla_1^2 = -\alpha^2/L^2$ where $\alpha = L\sqrt{\kappa_x^2+\kappa_y^2}$ and $D = Ld/dz$, $\partial/\partial t = \partial/\partial\tau\ (\mu_I\overline{\phi}/L^2) = \omega\,(\mu_I\overline{\phi}/L^2)$, $\partial/\partial x = \beta/L$, $z = \hat{z}L$, $f(z) = w_0(z)L/[\mu_I\overline{\phi}(z)]$, and $g(z) = \phi_0(z)/\overline{\phi}(z)$. All the exponential terms eventually cancel out, and we arrive at

$$\left[\frac{\omega}{\mathrm{Pr}} - (D^2-\alpha^2)\right](D^2-\alpha^2)f = -R\frac{d\bar{q}_f}{dz}\frac{L^3}{\epsilon\overline{\phi}}\alpha^2 g - R\frac{\overline{E}L}{\overline{\phi}}(D^2-\alpha^2)\alpha^2 g - S\hat{z}\beta(D^2-\alpha^2)f - 2S\beta Df, \tag{B15}$$

$$-\frac{\epsilon\overline{E}}{L^2}(D^2-\alpha^2)Dg + \frac{d\bar{q}_f}{dz}Dg + \frac{\epsilon\overline{\phi}}{L^3}\omega(D^2-\alpha^2)g + \frac{2\bar{q}_f}{L}(D^2-\alpha^2)g = \frac{d\bar{q}_f}{dz}f, \tag{B16}$$

where

$$R = \frac{\epsilon\bar{\phi}}{\mu\mu_I}, \quad \mathrm{Pr} = \frac{\mu}{\rho\bar{\phi}\mu_I}, \quad S = \frac{\rho\Gamma L^2}{\mu}. \tag{B17}$$

Equations (B15) and (B16) are linear equations of order four and three, respectively. Therefore, four boundary conditions for the initial velocity fluctuation, $w_0(z)$, and three boundary conditions for the initial potential fluctuation, $\phi_0(z)$, are required to obtain a unique solution. For the velocity fluctuation, we impose $w_0(z_0) = \partial w_0(z_0)/\partial z = 0$ and $w_0(z_0+L) = \partial w_0(z_0+L)/\partial z = 0$ based on no-slip boundary conditions and incompressibility of the fluid. For the potential fluctuation, it is assumed that the initial electric field fluctuations at the upper and lower boundaries are zero such that it is not violating Gauss's law, i.e., $\partial\phi_0(z_0)/\partial z = \partial\phi_0(z_0+L)/\partial z = 0$. The last boundary condition is determined by recognizing that the electrical conductivity decreases significantly with altitude in the lower atmosphere [37], and therefore we assume the lower boundary has much larger electrical conductivity than the upper boundary such that relatively the initial potential fluctuation at the lower boundary is negligible, i.e., $\phi_0(z_0) = 0$.

The boundary conditions are then transformed into the final dimensionless form: $f(z_0) = f'(z_0) = g(z_0) = g'(z_0) = 0$ for the lower boundary and $f(z_0+L) = f'(z_0+L) = g'(z_0+L) = 0$ for the upper boundary. To ensure numerical stability, we follow Appendix A in Schneider and Watson [38] to solve the ODEs numerically with these boundary conditions using a shooting method. We also observed that changing boundary conditions for the potential [e.g., employing a Neumann condition for the electric field $g''(z_0) = g''(z_0+L) = 0$] has little effect on the critical Rayleigh number.

[1] B. A. Tinsley, R. P. Rohrbaugh, M. Hei, and K. V. Beard, Effects of image charges on the scavenging of aerosol particles by cloud droplets and on droplet charging and possible ice nucleation processes, J. Atmos. Sci. **57**, 2118 (2000).

[2] F. Yu and R. P. Turco, From molecular clusters to nanoparticles: Role of ambient ionization in tropospheric aerosol formation, J. Geophys. Res.: Atmospheres **106**, 4797 (2001).

[3] S. N. Tripathi and R. G. Harrison, Enhancement of contact nucleation by scavenging of charged aerosol particles, Atmos. Res. **62**, 57 (2002).

[4] B. A. Tinsley, Scavenging of condensation nuclei in clouds: Dependence of sign of electroscavenging effect on droplet and CCN sizes, in *Extended Abstracts, 14th Conference on Cloud Physics and Precipitation* (ICCP, Bologna, Italy, 2004), pp. 248–252.
[5] M. J. Rycroft, S. Israelsson, and C. Price, The global atmospheric electric circuit, solar activity and climate change, J. Atmos. Sol. Terr. Phys. **62**, 1563 (2000).
[6] D. Siingh, V. Gopalakrishnan, R. P. Singh, A. K. Kamra, S. Singh, V. Pant, R. Singh, and A. K. Singh, The atmospheric global electric circuit: An overview, Atmos. Res. **84**, 91 (2007).
[7] W. A. Hoppel and S. G. Gathman, Charge transport through an aerosol cloud, J. Appl. Phys. **41**, 1971 (1970).
[8] R. Bruinsma and S. Alexander, Theory of electrohydrodynamic instabilities in electrolytic cells, J. Chem. Phys. **92**, 3074 (1990).
[9] G. Tomar, V. Shankar, A. Sharma, and G. Biswas, Electrohydrodynamic instability of a confined viscoelastic liquid film, J. Non-Newtonian Fluid Mech. **143**, 120 (2007).
[10] P. Atten, F. M. J. McCluskey, and A. C. Lahjomri, The electrohydrodynamic origin of turbulence in electrostatic precipitators, IEEE Trans. Ind. Appl. **IA-23**, 705 (1987).
[11] E. M. Lifshitz and L. P. Pitaevskii, *Physical kinetics* (Pergamon Press, Oxford, 1981).
[12] A. V. Timofeev and B. N. Shvilkin, Drift-dissipative instability of an inhomogeneous plasma in a magnetic field, Soviet Phys. Usp. **19**, 149 (1976).
[13] A. A. Galeev, S. S. Moiseev, and R. Z. Sagdeev, The theory of the stability of non-uniform plasma and anomalous diffusion, J. Nucl. Energy C **6**, 645 (1964).
[14] M. Di Renzo and J. Urzay, Aerodynamic generation of electric fields in turbulence laden with charged inertial particles, Nat. Commun. **9**, 1676 (2018).
[15] Y. Yao and J. Capecelatro, Competition between drag and Coulomb interactions in turbulent particle-laden flows using a coupled-fluid–Ewald-summation based approach, Phys. Rev. Fluids **3**, 034301 (2018).
[16] A. U. Karnik and J. S. Shrimpton, Mitigation of preferential concentration of small inertial particles in stationary isotropic turbulence using electrical and gravitational body forces, Phys. Fluids **24**, 073301 (2012).
[17] J. Lu, H. Nordsiek, E. W. Saw, and R. A. Shaw, Clustering of Charged Inertial Particles in Turbulence, Phys. Rev. Lett. **104**, 184505 (2010).
[18] J. K. Eaton and J. R. Fessler, Preferential concentration of particles by turbulence, Int. J. Multiphase Flow **20**, 169 (1994).
[19] S. Elghobashi and G. C. Truesdell, Direct simulation of particle dispersion in a decaying isotropic turbulence, J. Fluid Mech. **242**, 655 (1992).
[20] P. J. Ireland, A. D. Bragg, and L. R. Collins, The effect of Reynolds number on inertial particle dynamics in isotropic turbulence. Part 1. Simulations without gravitational effects, J. Fluid Mech. **796**, 617 (2016).
[21] J. P. L. C. Salazar, J. De Jong, L. Cao, S. H. Woodward, H. Meng, and L. R. Collins, Experimental and numerical investigation of inertial particle clustering in isotropic turbulence, J. Fluid Mech. **600**, 245 (2008).
[22] J. Chun, D. L. Koch, S. L. Rani, A. Ahluwalia, and L. R. Collins, Clustering of aerosol particles in isotropic turbulence, J. Fluid Mech. **536**, 219 (2005).
[23] M. R. Maxey, The gravitational settling of aerosol particles in homogeneous turbulence and random flow fields, J. Fluid Mech. **174**, 441 (1987).
[24] L. P. Wang and M. R. Maxey, Settling velocity and concentration distribution of heavy particles in homogeneous isotropic turbulence, J. Fluid Mech. **256**, 27 (1993).
[25] A. Aliseda, A. Cartellier, F. Hainaux, and J. C. Lasheras, Effect of preferential concentration on the settling velocity of heavy particles in homogeneous isotropic turbulence, J. Fluid Mech. **468**, 77 (2002).
[26] P. J. Ireland, A. D. Bragg, and L. R. Collins, The effect of Reynolds number on inertial particle dynamics in isotropic turbulence. Part 2. Simulations with gravitational effects, J. Fluid Mech. **796**, 659 (2016).
[27] K. A. Browning, T. W. Harrold, and J. R. Starr, Richardson number limited shear zones in the free atmosphere, Q. J. R. Meteorol. Soc. **96**, 40 (1970).
[28] A. A. Townsend, Excitation of internal waves in a stably-stratified atmosphere with considerable wind-shear, J. Fluid Mech. **32**, 145 (1968).

[29] K. H. Lloyd, C. H. Low, and R. A. Vincent, Turbulence, billows and gravity waves in a high shear region of the upper atmosphere, Planet. Space Sci. **21**, 653 (1973).
[30] P. Gualtieri, F. Picano, and C. M. Casciola, Anisotropic clustering of inertial particles in homogeneous shear flow, J. Fluid Mech. **629**, 25 (2009).
[31] C. Nicolai, B. Jacob, and R. Piva, On the spatial distribution of small heavy particles in homogeneous shear turbulence, Phys. Fluids **25**, 083301 (2013).
[32] M. H. Kasbaoui, D. L. Koch, G. Subramanian, and O. Desjardins, Preferential concentration driven instability of sheared gas–solid suspensions, J. Fluid Mech. **770**, 85 (2015).
[33] R. G. Harrison and M. H. P. Ambaum, Enhancement of cloud formation by droplet charging, Proc. R. Soc. London A **464**, 2561 (2008).
[34] L. Zhou and B. A. Tinsley, Production of space charge at the boundaries of layer clouds, J. Geophys. Res.: Atmospheres **112**, D11203 (2007).
[35] J. M. Rosen, D. J. Hofmann, and W. Gringel, Measurements of ion mobility to 30 km, J. Geophys. Res.: Atmospheres **90**, 5876 (1985).
[36] E. W. McDaniel and E. A. Mason, *The Mobility and Diffusion of Ions in Gases* (Wiley, New York, 1973).
[37] H. Volland, *Atmospheric Electrodynamics* (Springer-Verlag, New York, 1984).
[38] J. M. Schneider and P. K. Watson, Electrohydrodynamic stability of space-charge-limited currents in dielectric liquids. I. Theoretical study, Phys. Fluids **13**, 1948 (1970).
[39] J. Wang, W. B. Rossow, and Y. Zhang, Cloud vertical structure and its variations from a 20-yr global rawinsonde dataset, J. Climate **13**, 3041 (2000).
[40] J. C. Wyngaard and O. R. Coté, The budgets of turbulent kinetic energy and temperature variance in the atmospheric surface layer, J. Atmos. Sci. **28**, 190 (1971).
[41] L. Kelvin, Stability of fluid motion: Rectilinear motion of viscous fluid between two parallel plates, Philos. Mag. **24**, 188 (1887).
[42] M. H. Kasbaoui, R. G. Patel, D. L. Koch, and O. Desjardins, An algorithm for solving the Navier–Stokes equations with shear-periodic boundary conditions and its application to homogeneously sheared turbulence, J. Fluid Mech. **833**, 687 (2017).
[43] L. N. Trefethen, A. E. Trefethen, S. C. Reddy, and T. A. Driscoll, Hydrodynamic stability without eigenvalues, Science **261**, 578 (1993).
[44] E. R. Mansell and C. L. Ziegler, Aerosol effects on simulated storm electrification and precipitation in a two-moment bulk microphysics model, J. Atmos. Sci. **70**, 2032 (2013).
[45] O. Desjardins, G. Blanquart, G. Balarac, and H. Pitsch, High order conservative finite difference scheme for variable density low Mach number turbulent flows, J. Comput. Phys. **227**, 7125 (2008).
[46] J. Capecelatro and O. Desjardins, An Euler–Lagrange strategy for simulating particle-laden flows, J. Comput. Phys. **238**, 1 (2013).
[47] L. Schiller and A. Naumann, A drag coefficient correlation, Ver. Deutsch. Ing. Zeitung **77**, 318 (1935).
[48] S. B. Pope, *Turbulent Flows* (Cambridge University Press, Cambridge, 2000).
[49] J. Lowell and A. C. Rose-Innes, Contact electrification, Adv. Phys. **29**, 947 (1980).
[50] S. Matsusaka, H. Maruyama, T. Matsuyama, and M. Ghadiri, Triboelectric charging of powders: A review, Chem. Eng. Sci. **65**, 5781 (2010).
[51] H. Grosshans and M. V. Papalexandris, Direct numerical simulation of triboelectric charging in particle-laden turbulent channel flows, J. Fluid Mech. **818**, 465 (2017).
[52] X. Jin and J. S. Marshall, The role of fluid turbulence on contact electrification of suspended particles, J. Electrostatics **87**, 217 (2017).
[53] T. Gebhardt and S. Grossmann, Chaos transition despite linear stability, Phys. Rev. E **50**, 3705 (1994).
[54] A. Schmiegel and B. Eckhardt, Fractal Stability Border in Plane Couette Flow, Phys. Rev. Lett. **79**, 5250 (1997).
[55] B. Gayen and M. Alam, Algebraic and exponential instabilities in a sheared micropolar granular fluid, J. Fluid Mech. **567**, 195 (2006).
[56] P. Sagaut and C. Cambon, *Homogeneous Turbulence Dynamics* (Cambridge University Press, Cambridge, 2008).

[57] M. Malik, J. Dey, and M. Alam, Linear stability, transient energy growth, and the role of viscosity stratification in compressible plane Couette flow, Phys. Rev. E **77**, 036322 (2008).
[58] K. M. Butler and B. F. Farrell, Three-dimensional optimal perturbations in viscous shear flow, Phys. Fluids **4**, 1637 (1992).
[59] P. J. Schmid, Nonmodal stability theory, Annu. Rev. Fluid Mech. **39**, 129 (2007).
[60] E. J. Hinch, *Perturbation Methods* (Cambridge University Press, Cambridge, 1991).
[61] C. M. Bender and S. A. Orszag, *Advanced Mathematical Methods for Scientists and Engineers* (McGraw-Hill, New York, 1978).
[62] M. Malik, M. Alam, and J. Dey, Nonmodal energy growth and optimal perturbations in compressible plane Couette flow, Phys. Fluids **18**, 034103 (2006).